Three-dimensional behaviour of a prototype radioactive waste repository in fractured granitic rock.

Hywel R Thomas[1]

Philip J Vardon[2]

Peter J Cleall[1]

[1]Geoenvironmental Research Centre, Cardiff University

[2]Geo-Engineering Section, Department of Geoscience and Engineering, Delft University of

Technology

Corresponding author: Hywel R Thomas

Email: ThomasHR@Cardiff.ac.uk

Tel: 044 2920 874004

Fax: 044 2920 874004

Address: GRC, Cardiff School of Engineering, Cardiff University, The Parade, CF24 3AA,

UK

26 **Abstract:**

27 An investigation of the three dimensional coupled Thermo/Hydro/Mechanical behaviour of a

28 prototype repository in fractured granitic rock is presented. The pre-placement behaviour of

29 the repository is first considered, making use of a full three-dimensional simulation of the

30 problem. An effective continuum approach, augmented with discrete features with a high

31 hydraulic conductivity, is employed. The method adopted is found to be able to simulate

32 accurately the highly anisotropic flow regime observed at the pre-placement phase. The

33 major features of the full repository experiment under applied heating conditions were then

34 successfully simulated. The range of buffer hydration rates, the thermal response of the

35 repository and the associated mechanical response were successfully simulated. Approaches

36 to capture both the transient microstructural behaviour of the compacted bentonite (MX-80

37 type) and a MX-80 pellet material are incorporated. The repository behaviour was shown to

38 be strongly influenced by complex coupled processes, including interactions between the

39 system components. The adoption of a three dimensional modelling approach proved to be

40 essential in order to realistically simulate the behaviour of a repository incorporating

41 anisotropic flow behaviour. Finally potential impacts of the processes considered on

42 performance of the barrier system and in safety assessment are considered.

43

44

45

46

47

48

49

50

51

52

Notation:

54   *b*   parameter in soil water retention equation in table 2

55   C_{ps} heat capacity of solid

56   *G*   shear modulus

57   *k*   cohesion parameter

58   k_{init} initial hydraulic conductivity of the pellets

59   k_{inf} final hydraulic conductivity of the pellets

60   K_l unsaturated hydraulic conductivity

61   K_{feat} hydraulic conductivity of the features

62   K_{pel} hydraulic conductivity of the pellets

63   K_{sat} saturated hydraulic conductivity

64   K_{swell} hydraulic conductivity after water absorption

65   *M*   slope of the critical state line

66   *n*   porosity

67   p_0^* effective preconsolidation stress of a saturated soil

68   p_c reference stress

69   P_0 parameter in soil water retention equation in table 2

70   *r*   parameter controlling the maximum stiffness of the soil

71   *s*   suction

72   S_l degree-of-saturation

73   S_{labs} absorbed degree-of-saturation

74   S_{lA} the degree-of-saturation at which homogenisation of the pellets begins

75   *t*   time

76   Tr   transmissivity

77   *T*   temperature

78   **u**   displacement

79   u_a pore-air pressure

80	u_l	pore-water pressure
81	x,y,z	orthogonal directions
82	α	parameter in soil water retention equation in table 2
83	α_l	parameter representing the rate of movement of water between the macro and
84		micro structure
85	α_T	coefficient of thermal expansion
86	β	parameter controlling the increase of soil stiffness with suction
87	β_l	parameter in soil water retention equation in table 2
88	β_p	parameter representing the rate at which pellet homogenisation occurs
89	δ	parameter in unsaturated hydraulic conductivity equation in table 2
90	θ_{res}	residual water content
91	θ_{sat}	saturated water content
92	κ	elastic stiffness due to stress change
93	κ_s	elastic stiffness due to suction change
94	λ_T	thermal conductivity
95	$\lambda(0)$	plastic stiffness due to stress change
96	ρ_s	solid density
97	σ	stress in the direction of the subscript
98	τ	shear stress, plane defined by subscripts
99	υ	Poisson's ratio
100	ω_{abs}	parameter defining the proportion of absorbed pore-water
101	ω_{abs}^{max}	parameter defining the maximum proportion of absorbed pore-water
102	ω_{pel}	parameter representing the influence of homogenisation on the hydraulic
103		conductivity

104 **Keywords:** Numerical modelling, Partial saturation, Radioactive waste disposal, THM, 3D,

105 fractured rock.

1 Introduction

In recent years considerable progress has been reported in relation to an improved understanding of the coupled thermo/hydro/mechanical behaviour of unsaturated soils (e.g. Villar et al., 2005; Thomas et al., 2009). Such work has often been carried out as part of major international programmes of research directed towards the safe disposal of High Level Nuclear Waste (HLW). Indeed a number of papers have appeared in the recent literature comparing results from full scale experiments, carried out in underground research laboratories, with those from numerical simulations based on recent theoretical advances. This paper continues that pattern, now in the context of the "Prototype Repository" experiment carried out by Svensk Kärnbränslehantering AB (SKB), the Swedish Nuclear Fuel and Waste Management Company, at the Äspö Hard Rock Laboratory.

The Prototype Repository Project was instigated to investigate aspects of the repository system in an integrated manner (Svemar and Pusch, 2000). The project aims to replicate SKB's (Kärnbränslesäkerhet or Nuclear Fuel Safety) KBS-3 deep geological repository design in as realistic a set of conditions as possible, in respect to design, installation, geometry, materials, construction and environment. The exception is that the effects of HLW are simulated by use of heaters.

The hydraulic performance of a repository, prior to emplacement of the heaters, buffer material and backfill, is of importance as this represents both the boundary conditions of the buffer material and the 'initial conditions' of the post-placement system. The overall performance of a repository structure has been shown to be affected by its hydraulic performance (Thomas et al., 2003, 2009; Vardon et al., 2011). This hydraulic behaviour has been well characterised via inflow measurement and hydraulic tests using drilled boreholes (e.g. Rhén and Forsmark, 2001). This detailed dataset offers a valuable opportunity to investigate the behaviour of the system via numerical modelling.

133

134   The Thermo/Hydro/Mechanical (THM) behaviour of the repository is of importance for the

135   containment and isolation of the waste as well as the onset of other processes, such as gas

136   generation. The real behaviour is anisotropic and three-dimensional in nature and therefore

137   has been represented as such throughout this work. The hydraulic behaviour of the rock

138   provides the inflow of groundwater into the repository and therefore, in part, controls the

139   resaturation behaviour, a key aspect of the THM behaviour.

140

141   The Prototype Repository Project (PRP) is initially outlined in this paper, including the pre-

142   placement conditions and the experimental investigation of the rock. A three-dimensional

143   numerical simulation of the pre-placement conditions is then presented, which includes the

144   discrete fractures observed in the rock, allowing three-dimensional flow behaviour to be

145   simulated. The THM behaviour of the prototype repository was then investigated.

146

147   Previous attempts of work in this area have been presented by Cleall et al. (2006) and Chen

148   and Ledesma (2009). The former approach was able to realistically simulate pre-placement

149   infiltration into some deposition-holes but could not capture, in full, flows to all the holes.

150   Post-placement conditions were analysed with two dimensional THM and three dimensional

151   thermo/hydraulic simulations. Overall the temperature domain was well represented. Some

152   realistic hydraulic results were obtained and limited consideration of the mechanical field was

153   made. The key conclusions were that three dimensional modelling was essential, the

154   representation of the fractured nature of the rock was required and the pelletised material was

155   not well understood. Chen and Ledesma (2009) utilised an approach using different

156   hydraulic conductivities in the rock around each deposition-hole to allow for differing in-flow

157   rates. Simulated thermal results correlated well, but very limited hydraulic results were

158   presented. Whilst both sets of authors were able to simulate selected parts of the experiment

159   successfully they presented limited comparison of results and recognised the value of three-

160 dimensional simulations. In neither case were fully coupled three dimensional THM analyses

161 undertaken.

162

163 In this paper, the previous approaches are extended to encompass large-scale three

164 dimensional simulations, undertaken to represent the overall behaviour of the prototype

165 repository. For reasons of conciseness and space limitations, only selected results are

166 presented here, with the data presented designed to give an overview of the results achieved.

167 The THM model utilised in this work, COMPASS, has previously been presented in detail

168 (e.g. Thomas and He, 1997, 1998) and includes representation of coupled thermal, hydraulic,

169 air and mechanical processes. The governing equations are cast in terms of a primary

170 variable for each of the equations: pore-water pressure, u_l, temperature, T, pore-air pressure,

171 u_a, and displacement, $\mathbf{u}$. The principle of conservation of mass is used for the governing

172 equations of moisture and air flow, conservation of energy for the flow of heat and

173 equilibrium for the mechanical constitutive relations. Both liquid and vapour flow are

174 considered in the hydraulic governing equation, with vapour flow assumed to occur via

175 diffusion due to temperature driven vapour concentrations in the buffer. Numerical solution

176 of the governing equations is achieved via the finite-element method for spatial discretisation

177 and the finite-difference method for temporal discretisation. A parallel Bi-Conjugate

178 Gradient solver is used to solve the system of equations (Vardon et al., 2011), with a

179 predictor-corrector algorithm used to allow for material non-linearity.

180

181 **2 Prototype Repository Project**

182 The Prototype Repository Project (PRP) is a full-scale experiment designed to investigate the

183 thermo-hydro-mechanical behaviour of a HLW repository. The experiment is designed to be

184 more realistic than previous experiments (e.g. the Temperature Buffer Test (Hökmark et al.,

185 2005) and the Canister Retrieval Test (Thorsager et al., 2002) at Äspö Hard Rock Laboratory

186 (HRL); and the Buffer/Container Experiment (Thomas et al., 2009) and the Isothermal Test

187   (Thomas et al., 2003) at Atomic Energy of Canada's underground laboratory) and integrate

188   all aspects of the multi-barrier repository system including realistic setting within a real rock

189   mass at realistic depth. Consequently the experiment exhibits three-dimensional behaviour.

190   In addition, the timescale that the project is designed for, up to 20 years, is unique and may

191   yield important information regarding time-dependent behaviour. Importantly the experiment

192   is situated in fractured rock that exhibits anisotropic flow phenomena. This rock mass has

193   been characterised via boreholes and hydraulic tests. The PRP is well described by both

194   Svemar and Pusch (2000) and Johannesson et al. (2007). It is located at the edge of the HRL

195   facility at $450m$ below sea level. A schematic of the repository itself is shown in figure 1. It

196   is made up of two sections, one with four deposition-holes and the second with two, spaced

197   6m apart and drilled vertically and numbered from 1 to 6 as shown. The deposition-holes, as

198   indicated in figure 2, are filled sequentially with high density Wyoming bentonite blocks

199   (MX-80) surrounding the canister containing heaters at placement. Between the bentonite

200   blocks and the canister is initially a $10mm$ gap and between the bentonite and the rock is a

201   gap ($\sim 50mm$) which is filled with high density bentonite pellets. The tunnel and remaining

202     $1000mm$ of the deposition-holes contain backfill, which is a crushed rock and bentonite mix

203   (70/30% by weight). A concrete plug was constructed between the two sections and another

204   isolating the project from the rest of the tunnel complex. The plugs were designed to

205   withstand the stresses and pressures that the system was likely to create.

206

207   The pre-placement stage of the project starts with the construction of the tunnel and finishes

208   when emplacement of buffer material, backfill and canisters begins. Measurements have

209   been taken during this time period enable the rock to be characterised, numerical models to

210   be calibrated and give an indication of initial conditions. Rhén and Forsmark (2001) present

211   the collated data. The rock surrounding the PRP has been characterised at a relatively high

212   resolution. Thirty-nine boreholes were drilled, and in 33 of these detailed hydraulic

213   measurements were made. This has allowed the observation of both the characteristics of the

214   rock mass and the identification of specific features, such as local highly hydraulically

215   conductive fractures. In addition to the use of boreholes, the surface of the tunnel and

216   deposition-holes has been mapped and the hydraulically active areas identified. The inflow

217   rates into the tunnel and deposition-holes have also been monitored, with the results shown in

218   figure 3(a) and 3(b) respectively. The most important feature of these measurements is that

219   the inflow into Deposition-Hole 1 (DH-1) is much greater than into any of the others. Stress

220   measurements were also taken in one borehole to gain knowledge of the existing stresses with

221   the values reported in section 5.2.1.

222

223   The fractures in the tunnel have been mapped using various techniques e.g. standard

224   mapping, laser scanning, Borehole Image Processing System (BIPS) Television (TV)-logging

225   (unsuccessfully) and Ground Penetrating Radar (GPR) (Patel et al., 1997). Importantly, the

226   hydraulically active features have been identified (Patel et al., 1997). The deposition-holes

227   were mapped in the same manner; DH-3 was not identified to have any hydraulically bearing

228   fractures, unlike for example DH-1 and DH-5. A similar number of hydraulically bearing

229   fractures were identified in DH-1 and DH-5, with DH-1 having a significantly larger inflow

230   rate. A tentative conclusion can be drawn, that the majority of the flow occurs through these

231   hydraulic features and that the flow generally diffusing through the rock matrix is small in

232   comparison, although the rates through the fractures may highly variable. A fracture

233   mapping of the tunnel (after Rhén and Forsmark, 2001) is shown in figure 4 where all

234   fractures have been mapped and hydraulically active fractures identified. Two areas of large

235   inflows, denoted *Area 1* and *Area 2*, have been identified and shaded. A more complete

236   overview of the drilling and testing regime can be found in Rhén and Forsmark (2001).

237

238   Following the mapping, drilling and hydraulic tests the transmissivity of the rock and

239   hydraulic connectivity was estimated and a number of key hydraulic features hypothesised by

240   Rhén and Forsmark, (2001). These are detailed in Table 1 and diagrammatically included in

9

241 the domain visualisation in figure 5. It has been initially hypothesised by Rhén and Forsmark

242 (2001) that these features have circular shapes, with the coordinates quoting the centre of the

243 feature. Alternative shapes have not been utilised and may affect the results, due to the

244 change in surface area and connectivity with other model features. However, analysis of this

245 aspect is beyond the scope of the work. The fact that some deterministic features have been

246 identified does not, by default, suggest that the remainder of the rock mass is not fractured,

247 but only that during the tests, significant identifiable preferential flow directions have not

248 been recognised in those regions. The sampling process uses a discrete number of boreholes

249 to identify these features and as such, some features are likely to be missed, but those of

250 reasonable size and proximity to the tunnels are likely to have been identified.

251

252 *Area 2*, highlighted on the tunnel fracture map, figure 4, shows a region with a well defined

253 fracture which is hydraulically active and coincides with the intersection between the tunnel

254 and the proposed South major fracture. However, *Area 1*, highlighting a large water flow

255 into the tunnel and another well defined fracture, via surface fracture mapping, does not

256 coincide with any deterministic feature proposed by Rhén and Forsmark (2001), although is

257 close to the South major fracture and it is possible that it may have some interaction. An

258 additional feature of hydraulic conductivity is proposed to allow the impact of increased

259 permeability in this region to be assessed, for convenience named *Region 1*.

260

261 In the post-emplacement phase each of the deposition-holes, contains a copper canister

262 inclusive of iron over-pack and heaters, compacted MX-80 bentonite buffer and pelletised

263 MX-80 buffer material. The configuration is shown in detail in figure 2. The tunnel is

264 backfilled with a mixture of crushed rock and bentonite and sealed between sections 1 and 2

265 and at the end by means of a concrete plug. A large quantity of data has been collected

266 during the post-emplacement phase of the experiment (e.g. Goudarzi and Johannesson, 2007).

267 Figures 6 and 7, for example, show data collected from DH-1 and DH-3. The highly

268   anisotropic and locally varied flow, apparent in the deposition tunnel and holes during the

269   pre-placement stage, results in the buffer in DH-1 resaturating at a faster rate than other

270   deposition-holes (Johannesson et al., 2007). All deposition-holes exhibit water content

271   variations from a hot dry side to a cooler wet side of the buffer, before full saturation. The

272   thermal response is driven by the heat flux from the canisters with peak temperatures located

273   in DH-1 in the centre of section 1. In general, peak temperatures for drier deposition-holes

274   are higher than for wetter deposition-holes, as expected. Swelling pressures increase with

275   hydration, rising to up to $\sim 7MPa$ in locations where full saturation has occurred. However

276   observed patterns in pressure development are complex and their reliability has been

277   questioned due to possible arching effects, local contact and stress cell installation (e.g. Chen

278   and Ledesma, 2009). Finally, in the backfill a trend of saturation has been measured, with the

279   fastest rates found close to DH-1.

280

281   **3 Simulation approach**

282   **3.1 Domain**

283   The information from the site data and the modelling strategy have been used to create a

284   geometric model of the domain for the pre-emplacement condition i.e. an empty tunnel and

285   deposition-holes within a rock mass, shown in figure 1, with the whole domain shown in

286   figure 5(a) and details of the fractures and Region 1 shown in figure 5(b) – 5(d). The domain

287   has been chosen to extend approximately $50m$ away from the repository in all directions, to

288   ensure the effective deployment of the boundary conditions. To check that this is achieved

289   the hydraulic flux has been monitored at the domain edge. In addition, a single analysis has

290   been undertaken with a domain $100m$ away from the repository in all directions with only

291   negligible differences in any results (less than 1%); this has not been presented in this paper.

292   The total domain size is therefore $100 \times 100 \times 160m$ with the $160m$ dimension being along

293   the length of the tunnel. Linear tetrahedral elements have been used, allowing for irregular

294   shapes and enabling areas of complex geometry and great spatial variation of results to be

295   modelled with a fine mesh resolution, while areas which are expected to have little variation

296   of results and less complex geometry can have a significantly coarser mesh resolution. When

297   discretised the model has 484,954 tetrahedral elements and 86,414 nodes for the pre-

298   placement conditions and 920,983 elements with 163,240 nodes for the post-placement, this

299   mesh has been checked for spatial convergence.

3.2 Material parameters

301   Material parameters and material behaviour relationships are summarised in table 2. As

302   noted by Chen and Ledesma (2009), gas pressures are likely to be small as temperatures are

303   not anticipated to be higher than 80 $°C$ so advective gas transport is neglected. Where gas or

304   pore-air pressures are required in the formulation a constant of atmospheric pressure is used.

3.2.1 The host rock

306   The host rock is a complex fractured material made up from, in the main, Äspö Diorite. The

307   material is highly fractured with fractures and joints generally filled with chlorites, calcite

308   and epidote and considered tight (Patel et al., 1997). The average density is 2770 kg/m^3 with

309   the porosity reported as being 0.005±0.002 (Dahlström, 1998; Patel et al., 1997). Discussion

310   of hydraulic material parameters for the crystalline rock in the Äspö area where the PRP is

311   situated is well documented (for example summarised by Rhén and Forsmark, 2001). The

312   parameters required for the analysis are the hydraulic conductivities of the 'intact rock', that

313   is the rock matrix including the background distribution of fractures, and the hydraulic

314   conductivity of the identified hydraulically conductive features and the associated porosities.

315   The rock is considered to be saturated throughout the pre-emplacement stage therefore no

316   variation with degree-of-saturation is required. The values of hydraulic conductivity for the

317   'intact rock' were found, via experimentation, to have a wide range and were spatially

318   variable. The range of values was found to be from 10^{-5} to 10^{-13} m/s. It has been conjectured

319   that the conductivity will be anisotropic due to geological processes (Rhén and Forsmark,

320   2001), however statistical confidence limits do not observe significant differences at the 90

321   percentile confidence limit (Vardon 2009). Other works show similar findings and wide

322   range of possible hydraulic conductivities, e.g. Rhén et al. (1997). A conductivity, at the

323   lower end of the mid-range of experimentally determined conductivities, of $5x10^{-12}$ *m/s* will

324   be used and the more significant deterministic hydraulic features included explicitly.

325

326   The hydraulic features have been represented as areas of higher hydraulic conductivity than

327   the bulk rock mass. These higher hydraulic conductivities have been calculated from

328   transmissivities (Rhén and Forsmark, 2001), using a standard fracture thickness for modelling

329   purposes of 0.1*m* for the major fractures and 0.05*m* for the minor fractures. The derived

330   values of hydraulic conductivity for the fractures are summarised in table 1. It should be

331   noted that the fracture thicknesses, whilst reasonable, are arbitrary and serve only to allow

332   representation of the fracture. There is little evidence to indicate the size or transmissivity of

333   the identified region of high hydraulic inflow into the tunnel, *Region 1*, therefore, a region

334   has been included within the geometric model, with the hydraulic conductivity of the major

335   fractures. Unsaturated hydraulic conductivity and water retention behaviour, incuding

336   parameterisation, is based upon the approach of Gens et al. (1998) for granite. A heat

337   capacity of 750 *J/kgK* is adopted, based upon Patel et al. (1997), and Dahlström (1998)

338   quotes the thermal conductivity as a constant 2.5 *W/mK*. A linear elastic mechanical model is

339   utilised for the host rock due to the relatively low stresses applied from the buffer material.

340   For Poisson's ratio, *v,* and shear modulus, *G*, values of 0.25 and 27,600 *MPa* are adopted

341   (Delin et al., 1995; Stille and Olsson, 1996).

342   **3.2.2 MX-80 bentonite**

343   The buffer material is highly-compacted sodium bentonite clay, known as MX-80. Blocks of

344   buffer material were installed in rings, cylinders and bricks depending on location. They are

345   designed to give a homogenised pattern of final dry density after rehydration and swelling.

346   The installed average porosities were 0.4, 0.36 and 0.38 for the cylinders, rings and bricks,

347   respectively (Börgesson et al., 2002). The heat capacity and thermal conductivity of MX-80

348   were determined by Börgesson and Hernelind (1999), with the heat capacity reported as 800

349   *J/kgK*. The thermal conductivity, λ_T, (*W/m/K*) was found to vary with degree-of-saturation,

350   S_l, as:

$$
\begin{aligned}
\lambda_T &= 0.3 & S_l &\leq 0.2 \\
\lambda_T &= 1.5S_l & 0.2 &< S_l \leq 0.8 \\
\lambda_T &= 0.8 + 0.5S_l & 0.8 &< S_l \leq 1.0
\end{aligned}
\tag{1}
$$

352   An elasto-plastic model (Alonso et al., 1990) has been adopted to represent the mechanical

353   behaviour of the bentonite. The elastic and plastic stiffness due to stress change, κ and $\lambda(0)$,

354   were found based upon experimental evidence collated by Pusch (2001) after Börgesson et al.

355   (1993) as 0.0245 and 0.238. The parameters for the relationship defining plastic stiffness for

356   any suction ($s = u_a - u_w$), r and β, were found experimentally by Lloret et al., (2003) to be 0.9

357   and 1.0 respectively. Following Alonso et al. (1990) the reference stress, p_c, was defined as

358   atmospheric pressure. The effective preconsolidation stress of a saturated soil, p_0^*, is

359   estimated based on the maximum preconsolidation pressure applied to the sample during

360   construction of the blocks (100*MPa*) and the initial suction yielding a value of approximately

361   45*MPa*. The mechanical behaviour of bentonite due to suction is based upon work

362   undertaken by Lloret et al. (2003). The elastic stiffness due to suction change, κ_s, was found

363   to be 0.075 with little or no plastic behaviour exhibited in the suction range considered (up to

364   500*MPa*). Therefore the suction yield surface was not considered. A shear modulus, G, of

365   10*MPa* is adopted following Cleall et al. (2006). Following experiments undertaken by

366   Börgesson et al. (1995) the slope of the critical state line, M, can be shown to be 0.358, with a

367   first estimate of the cohesion parameter, $k=5.6\times10^{-3}$, based on the approximate cohesion of

368   56*kPa* with the samples at approximately $1\times10^7 Pa$ suction. Limited thermal expansion will

369   take place, based largely on the amount of water in the sample (Börgesson et al., 1995). As

370   this is likely to be significantly less that the expansion due to suction a constant based on

371   average water content is used of, thermal expansion, $\alpha_T=1\times10^{-4}\ K^{-1}$. A saturated hydraulic

372   conductivity, determined from experimental results by Börgesson and Hernelind (1999) and

373   Villar et al. (2005) has been employed. The moisture-retention behaviour is represented using

374   a van Genutchen relationship fitted to experimental data presented by Börgesson and

375   Hernelind, (1999).

376   **3.2.3 MX-80 pellets**

377   Very limited experimental data exists for MX-80 pellets. Hoffmann et al. (2007) presented a

378   series of experiments exploring the hydro-mechanical behaviour of such pelletised materials

379   and these have been further investigated more recently by Alonso et al. (2011). For

380   mechanical model parameters Hoffman et al. (2007) presented some initial results and

381   recommends an increase in stiffness with application of stress. A sensitivity analysis for $\lambda(0)$

382   has been undertaken using experimental results from the Canister Retrieval Test (CRT)

383   (Thorsager et al., 2002) yielding a value of 0.6 for the homogenised pellet region. In the

384   absence of other data, thermal behaviour will be assumed to be similar to that of the MX-80

385   bentonite buffer material.

386   **3.2.4 Backfill**

387   The backfill material is a mixture of crushed rock from the tunnel excavation (70%) and

388   bentonite (30%) and is installed in compacted layers (Johannesson et al., 2007). The

389   bentonite is a converted sodium bentonite originating from Milos, Greece. The water content

390   at installation was 12% and a porosity of 0.363 was determined consistent with the dry-

391   density of 1.65g/cm^3 (Börgesson et al., 2002). The saturated hydraulic conductivity was

392   found to be $1.5 \times 10^{-10} m/s$ (Johannesson et al., 1999), with the relationship for the unsaturated

393   variation of hydraulic conductivity shown in table 2 used for backfill with the value δ=10

394   found to correlate well with experimental data (Börgesson and Hernelind, 1998).

395   Experimental water-retention data presented by Börgesson and Hernelind (1999) have been

396   fitted to a van Genutchen relationship. A saturated thermal conductivity of 1.5$W/m/K$ is

397   employed (Börgesson and Hernelind, 1999) with a similar form of variation with water

398   saturation to MX-80 assumed:

$$\lambda_T = 0.3 \qquad\qquad\qquad S_l \le 0.2$$

$$\lambda_T = 0.3 + \frac{11}{6}(S_l - 0.2) \qquad\quad 0.2 < S_l \le 0.8 \qquad (2)$$

$$\lambda_T = 1.0 + 0.5 S_l \qquad\qquad 0.8 < S_l \le 1.0$$

399

400 Limited mechanical data is available for the backfill, e.g. Mata (2003), however this is for a

401 mixture of MX-80 bentonite and rock. Oedometer experiments presented were found to give

402 $\kappa=0.016$ and $\lambda(0)=0.102$. Due to a lack of similar experimental evidence in suction

403 controlled conditions the values of M, r and β will be assumed to be consistent with the MX-

404 80. Volume changes with respect to suction change, κ_s are assumed to be governed by the

405 clay volumetric fraction, i.e. 30%, and the coefficient of thermal expansion, α_T, consistent

406 with the volumetric fractions of rock and clay, i.e. 30% clay and 70% rock.

407

408 **4 Transient flow behaviour of bentonite**

409 **4.1 MX-80 bentonite**

410 A number of investigations of coupled THM behaviour of in-situ tests (Thomas et al 2003,

411 2009) have demonstrated a requirement to incorporate the impact of microstructural

412 behaviour within compacted bentonite barriers. In those studies an approach of 'choking'

413 moisture flow in confined conditions on increasing saturation was found to significantly

414 improve the results. In this study this approach is further developed to represent the effect of

415 transient microstructural behaviour on hydraulic flow (Vardon, 2009). A number of

416 processes impacting the flow behaviour of compacted bentonite can be identified and include

417 i) time required for free and microstructure absorbed water to reach equilibrium; ii)

418 availability of free water to allow microstructural swelling; iii) ageing of manufactured

419 bentonite resulting in a reduction in the proportion of macro-pores; iv) impact of flow-rate

420 and swelling on the creation, enlargement or healing of preferential pathways for flow; and v)

421 the confinement conditions (Tang and Cui, 2005; Dueck, 2008; Delage et al., 2006; Cui et al.,

422 2008). The approach presented by Thomas et al. (2003, 2009) has been applied, via

16

423 numerical modelling, when flow-rates are relatively slow. In those studies instantaneous

424 equilibrium is assumed with a fixed proportion of water absorbed into the micro-pores. The

425 impact of faster in-flow rates where microstructural swelling takes place at a different time

426 scale may have not been captured using that approach. The work presented here includes a

427 methodology which more fully captures the process of microstructural swelling at the faster

428 macro flow rates.

429 **4.2 Pelletised MX-80 bentonite**

430 For the hydraulic conductivity of pelletised bentonite, Hoffmann et al. (2007) presented two

431 relationships based on fast and slow infiltration. It can be noticed that initially the inter-pellet

432 voids dominate and as the pellets expand the hydraulic conductivity is reduced; therefore the

433 rate of pellet expansion is the limiting factor. For slow infiltration the pellets are able to

434 expand as water flows and the conductivity will reduce; whilst for rapid infiltration the pellets

435 will not initially have time to expand and the conductivity will remain high until enough time

436 has passed to allow pellet expansion. A similar observation is made by Alonso et al. (2011).

437 In an attempt to capture this behaviour an initial approach is presented here to represent

438 transient change in conductivity as the pellet region hydrates based on the assumptions that i)

439 inter-pellet pores initially dominate during the saturation process, ii) an initial hydraulic

440 conductivity exists based upon the mean pellet size, pellet-size distribution and pellet

441 compaction, iii) a final hydraulic conductivity exists, based upon the final homogenised

442 structure, iv) only monotonic wetting paths are considered, and v) above a specified degree-

443 of-saturation the pellet region moves towards a homogenised state at a constant rate. In this

444 study an approach is utilised to represent the effect of transient behaviour on hydraulic flow

445 (Vardon, 2009), with the material relationships defined in table 2.

446

447 To investigate the proposed model of the pelletised MX-80 a series of analyses of the

448 Cannister Retrieval Test has been undertaken (Vardon, 2009). From these tests a set of

449 calibrated parameters for the pelletised region have been obtained ($k_{init}=1\times10^{-10}m/s$,

450 $k_{inf}=1\times10^{-16}m/s$, $\beta_p=1\times10^{-7}s^{-1}$, and $S_{lA}=0.3$). In the absence of experimental data, the

451 moisture-retention curve for compacted MX-80 has been adopted.

452

453 **5 Simulations**

454 **5.1 Pre-Placement Simulation**

455 The simulation performed includes all the identified hydraulic features identified in section 2,

456 including the region of high hydraulic conductivity (*Region 1*). The hydraulic conductivities

457 are based upon the transmissivities quoted by Rhén and Forsmark (2001), or the central

458 figure when a range is quoted. The analysis was run for 2 years, at which point a pseudo

459 steady-state had been achieved, where the rate of change in inflow into the deposition-holes

460 and tunnel system is found to be less than 1%. The mesh has been checked for spatial

461 convergence and the time step for temporal convergence.

462 **5.1.1 Initial and boundary conditions**

463 The reported inflow rates, shown in figure 3(a) and 3(b), show little variation over the time

464 they were recorded (Rhén and Forsmark, 2001). Although the construction of the tunnel was

465 undertaken over time, the initial conditions for this simulation were assumed to be hydrostatic

466 with the mean sea level. Boundary conditions on the far field have been maintained at

467 hydrostatic pore-water pressure. The distance the boundary is set from the repository has

468 been found not to affect the results through monitoring of the boundary fluxes. On the

469 interior of the tunnel and deposition-holes, following the approach of Thomas et al. (2009),

470 the pore-water pressure has been fixed at zero to reflect the atmospheric pressure. This was

471 also found experimentally, e.g. Mishra et al. (2008).

472 **5.2 Post-Placement Simulations**

473 **5.2.1 Boundary conditions and initial condition**

474 On the outer boundaries the temperature is fixed at the initial value, the pore-water pressure is

475 fixed at hydrostatic pore-water pressure with the exception of the far boundary which the

476 tunnel intersects, where a zero moisture flux boundary condition was applied. The

18

477 deformation domain is fixed normal to the boundary at the outer edge. At the boundary of

478 the canister/buffer interface, a zero moisture flux condition was applied with deformation

479 normal to the canister surface restrained. A heat flux was applied on the surface of the

480 canister based upon the total energy provided to the heater. Initially the temperature is set to

481 289K throughout the domain, based upon initial experimental evidence. The stress conditions

482 in the rock mass as recorded and resolved in coordinates orthogonal to the repository are:

483
$$\begin{Bmatrix} \sigma_x \\ \sigma_y \\ \sigma_z \\ \tau_{xy} \\ \tau_{yz} \\ \tau_{zx} \end{Bmatrix} = \begin{Bmatrix} 22.9 \\ 17.8 \\ 24.5 \\ 4.5 \\ 6.7 \\ 23.5 \end{Bmatrix} MPa \tag{5}$$

484 where x is along the tunnel length, y is vertical and z is perpendicular to both x and y. The

485 initial pore-water pressure in the buffer and backfill material was based upon the water

486 content and degree of saturation reported from installation measurements by Börgesson et al.

487 (2002) and Johannesson et al. (2004) and the retention properties presented in table 2. The

488 compacted bentonite cylinders and rings were found to have an initial pore-water pressure of

489 -64.7 and -49.2MPa respectively (based upon degrees of saturation of 0.79 and 0.86

490 respectively), with the bricks and pellets -112 and -111MPa (degrees of saturation of 0.64

491 and 0.25 respectively).

492

493 **6 Results**

494 A single simulation has been undertaken for the pre-placement phase, where the proposed

495 model inclusive of deterministic features has been implemented. Data from the simulations is

496 compared with the salient experimental evidence, namely the inflow rate along the repository

497 tunnel, shown in figure 3(a), the inflow rates in the deposition-holes, shown in figure 3(b) and

498 a contour plot of the pore-water pressure along the centre-line is shown in figure 8. This

499 analysis can be seen, by consideration of figure 3(a), to simulate the inflow into the tunnel

500   closely. Importantly there is good qualitative trends displayed, with a great difference in

501   inflow rate at chainages above and below 3 588m. Considering the flow into the deposition-

502   holes, seen in figure 3(b), this analysis is able to simulate the flows into DHs 2-6, with the

503   numerical results following the experimental results closely. The simulated inflow into DH-1

504   is approximately only 12% of the experimental value, however it is significantly higher than

505   that simulated for DHs 2-6 showing a trend that is in agreement with the experimental results.

506   Simulation of the inflow into DH-1 could be quantitatively improved by altering the

507   hydraulic conductivities in the model, however such a modification would require a priori

508   knowledge of the inflows; also this does not guarantee that this is the correct mechanism. For

509   example, the same result could also be achieved by increasing the size of the closest fracture;

510   therefore the parameters derived from experimental data have continued to be used.

511

512   Figure 8, highlights the effects of the major features. The edge of the major fracture,

513   indicated in the figure, can be seen between DH-1 and the end of the tunnel. The effect of

514   this feature can be seen by the extended contour of approximately 1MPa, extending vertically

515   from the repository tunnel.

516

517   Results for the initial operational phase of the post-placement analysis, i.e. up to 10 years, are

518   presented in figures 6, 7 and 9-12, when the thermal and hydraulic gradients are at their

519   greatest, due to the greatest heat output from the canisters and the initially unsaturated state of

520   the bentonite. In this time the peak temperature is likely to be found, as the heat output is the

521   greatest, and therefore the moisture regime will be greatly influenced by the heat distribution.

522   The post-placement results are presented at mid-height of the buffer, although they have also

523   been compared in other locations. The temperature results for DH-1 and DH-3 are shown in

524   figures 6(a) and 7(a), with the numerical results correlating well with the experimental

525   results. Examining the temperature contour plot shown in figure 9, the temperature fields

526   from the deposition-holes can be seen to 'interact' increasing the temperature, demonstrating

20

527   that a three-dimensional analysis is essential. Consequently, the temperature exhibited by

528   DH-3 is higher than that of DH-1, as expected by its position in the PRP. The relative

529   humidity results for DH-1 and DH-3 are shown in figures 6(b) and 7(b). In DH-1, it is seen

530   that the numerical results simulate the experimental behaviour well. It is noted that the effect

531   of the fracture seen in the contour plots in figure 10 creates a large spatial gradient and the

532   results are therefore sensitive to the exact sensor location and subtleties of the

533   fracture/deposition-hole interaction. A possibly significant difference is that the inner-most

534   sensor location, sensor WBU10013 at $0.585m$ radius, does not saturate as quickly as shown

535   experimentally and therefore allows vapour transport to continue. It is not clear if this

536   location is saturated experimentally as the sensor has stopped working. Significantly for long

537   term simulations, the gradients of re-saturation shown in the simulations are almost identical

538   to that shown by all the sensors experimentally when they fail or at the final recording. In

539   figure 7(b) the numerical results correlate well to the experimental results, with a slight

540   overestimation of re-hydration, but exhibiting good qualitative trends. The final gradients

541   shown experimentally are also reproduced well in the simulation. Figures 6(c) and 7(c)

542   present the mechanical evolution in terms of net mean stress for both experimental and

543   numerical results. The numerical results are reasonable in stress magnitude and importantly,

544   differences in magnitudes correlate well with experimental results. The results also correlate

545   with the hydraulic behaviour, that is, where significant hydration has occurred stresses due to

546   swelling have occurred. The increase in stresses noted after approximately 2,000 days is due

547   to the increase in saturation shown by the model at this point, which is driven by a reduction

548   in heat output from the canisters.

549

550   Figures 9-11 present contour plots at vertical cross-sections through the centre-line of the

551   tunnel for the temperature, pore-water pressure and displacement. Figure 9 shows the

552   thermal interaction between the DHs and shows the transient thermal behaviour as well as a

553   power failure in DH-2. It can be seen in figure 10 that the backfill largely saturates over the

554   first 2,500 days, which is in agreement with the experimental results (Goudarzi and

555   Johannesson, 2007). The backfill behaves as a relatively large water sink in this period. It

556   can also be seen that the resaturation behaviour in DH-1 is local to the fracture and that at the

557   top and the bottom of the buffer the qualitative trend is similar to that of DH-3, as exhibited

558   experimentally. In figure 11 the displacement results indicate that the swelling in the

559   compacted buffer will cause lateral movement towards the pellets, as expected, and also a

560   displacement towards the tunnel into the backfill material. This displacement, however, does

561   not cause the buffer material to penetrate the tunnel. Figure 12 shows a pore-water pressure

562   contour-plot on a horizontal cross-section through the tunnel, highlighting the impact of the

563   major fractures on the pore-pressure surrounding the tunnel.

564

565   **7 Discussion**

566   The model results illustrate that the early stage (e.g. 5 years) the thermo-hydro-mechanical

567   behaviour can be well reproduced. This gives confidence that such models can be utilised in

568   safety assessment. Longer term behaviour, such as extrapolation to hundreds of years is less

569   certain. Therefore long-term experimentation remains extremely valuable. It is noted that

570   the model relies on accurate and detailed geological characterisation and that the accurate

571   performance of the system cannot be modelled using two-dimensional or averaged material

572   parameters. A model such as this could be further utilised to give a proportion of behaviour,

573   in   terms   of,   for   example,   the   number   of   deposition-holes   having   a   certain

574   saturation/temperature/stress, which may therefore give an indication of system performance

575   in terms of reliability.

576   Such an early stage (pre-saturation) model is useful as it is during this time that heat output is

577   highest, and also thermal conductivity is the lowest, therefore design limits based on

578   temperature will require such models, so as not to be overly conservative. Furthermore the

579   recent development of THM models to include consideration of chemical species (e.g. Cleall

580   et al., 2007; Gens, 2010) and the impact of advective processes on the geochemical

581 conditions close to the canister (Thomas et al., 2012; Cleall et al., 2013; Masum et al., 2013)

582 and the potential for enhanced corrosion and gas production highlights the need for

583 confidence in the correct representation of moisture and gas movement in the short-term near

584 field behaviour of repository systems. It is noted that the model requires a large number of

585 material parameters to be determined. However, a large proportion are for the expansive

586 clay, which is part of the engineered barrier. This means that material variability is able to be

587 controlled and is likely to be low, therefore these do not pose an undue burden on the

588 operator of such a programme. The parameters for the rock are significantly fewer with the

589 permeability being one of the most variable and also influential, as it is from here that water

590 is supplied to the buffer/backfill material.

591

592 **8 Conclusions**

593 A model of the prototype repository system has been presented, based upon a fully three-

594 dimensional finite-element formulation. This allows for the inclusion of inherent anisotropy

595 due to the existence of fractures. In particular the local influences of known fractures are

596 included. The pre-placement stage has first been modelled, where large variations in inflow

597 rate have been captured. It has been demonstrated that the hydraulic performance is

598 inherently three-dimensional and should be modelled as such to gain meaningful results.

599 A three-dimensional Thermo/Hydro-/Mechanical (THM) investigation is then presented. The

600 key aspects of the THM behaviour of the repository are well captured by the modelling

601 strategy, namely: i) three-dimensional behaviour in the thermal, hydraulic and mechanical

602 fields; ii) close correlation of numerical result of the thermal field with experimental values;

603 iii) backfill hydration similar to that reported experimentally; iv) drying of buffer material

604 close to heaters and wetting adjacent to rock reproduced; v) anisotropic hydration behaviour

605 reproduced; and vi) swelling pressure increases with hydration, with differences in

606 magnitudes represented. The temperature field was noted to be intrinsically three-

607 dimensional, with the effects of adjacent canisters' heat output influencing the temperature

608 within other deposition-holes. The hydraulic importance of the fracture intersecting DH-1

609 was highlighted and the highly three-dimensional anisotropic hydration behaviour noted and

610 reproduced. The significance of the backfill as a substantial sink for pore-water was

611 demonstrated with the simulations able to largely reproduce the saturation time exhibited

612 experimentally with the geological supply of water was critical to the hydration rate of

613 various aspects of the repository.

614

620

621 **10 References**

622 Alonso, E.E., Gens, A., and Josa, A., (1990) "A constitutive model for partially saturated

623 soils", *Géotechnique*, 40(3), 405-430.

624 Alonso, E.E., Romero, E., and Hoffmann, C., (2011) "Hydromechanical behaviour of

625 compacted granular expansive mixtures: experimental and constitutive study", *Géotechnique*,

626 61(4), 329-344.

627 Börgesson, L., Gunnarsson, D., Johannesson, L-E., and Sandén, T., (2002) *Äspö Hard Rock*

628 *Laboratory, Prototype Repository, Installation of buffer, canisters, backfill and instruments*

629 *in section 1*, SKB, IPR-02-23, Stockholm.

630 Börgesson, L., and Hernelind, J., (1998) *Preparatory modelling for the backfill and plug test*

631 *- Scoping calculations of H-M processes*, SKB, IPR-99-11, Stockholm.

632 Börgesson, L., and Hernelind, J., (1999) *Preliminary modelling of the water saturation phase*

633 *of the buffer and backfill materials*, SKB, IPR-00-11, Stockholm

634 Börgesson, L., Johannesson, L-E., and Fredrikson, A., (1993) *Laboratory investigations of*

635 *highly compacted bentonite blocks for buffer material Compaction technique and material*

636 *composition*, SKB, PR 44-93-010, Stockholm.

637 Börgesson, L., Johannesson, L-E., Sandén, T., and Hernelind, J., (1995) *Modelling of the*

638 *physical behaviour of water saturated clay barriers, Laboratory tests, material models and*

639 *finite element application*, SKB, TR-95-20, Stockholm.

640 Chen, G.J., and Ledesma, A., (2009) "Coupled thermohydromechancial modeling of the full-

641 scale in situ test "prototype repository", *Journal of Geotechnical and Geoenvironmental*

642 *Engineering*, 135(1), 121-132.

643 Cleall, P.J., Melhuish, T.A., and Thomas, H.R., (2006). "Modelling the three-dimensional

644 behaviour of a prototype nuclear waste repository", *Engineering Geology*, 85(2), 212-220.

645 Cleall, P.J., Seetharam, S.C., and Thomas, H.R., (2007) "Inclusion of some aspects of

646 chemical behaviour of unsaturated soil in thermo/hydro/chemical/mechanical models. I:

647 Model development", *ASCE Journal of Engineering Mechanics*, 133(3), 338-347

648 Cleall, P.J., Singh, R.M., and Thomas, H.R., (2013) "Vapour transfer in unsaturated

649 compacted bentonite", *Géotechnique*, 63(11), 957-964.

650 Dahlström, L-O., (1998) *Äspö HRL - Test plan for the Prototype Repository*, SKB, HRL-98-

651 24, Stockholm.

652 Delage, P., Marcial, D., Cui, Y.J., and Ruiz, X., (2006) "Ageing effects in a compacted

653 bentonite: a microstructure approach", *Géotechnique*, 56(5), 291-304.

654 Delin, P., Sturk, R., and Stille, H., (1995) *Laboratory testing of rock*, SKB, Technical note

655 25-95-08v.

656 Gens, A., Garcia-Molina, A.J., Olivella, S., Alonso, E.E., and Huertas, F., (1998) "Analysis

657 of a full scale in situ test simulating repository conditions", *International Journal for*

658 *Numerical and Analytical Methods in Geomechanics*, 22, 515-548.

659 Gens, A., (2010) "Soil–environment interactions in geotechnical engineering", *Géotechnique*,

660 60(1), 3-74.

661   Goudarzi, R., and Johannesson, L-E., (2007) *Äspö Hard Rock Laboratory, Prototype*

662   *Repository, Sensors data report (Period 010917-070601)*, Report No: 17, SKB, IPR-07-19,

663   Stockholm.

664   Hoffmann, C., Alonso E.E., and Romero, E., (2007) "Hydro-mechanical behaviour of

665   bentonite pellet mixtures", *Physics and Chemistry of the Earth*, 32, 832-849.

666   Hokmark, H., Borgesson, L., and Hernelind, J., (2005) *Äspö Hard Rock Laboratory,*

667   *Temperature Buffer Test, Scoping design calculations*, SKB, IPR-05-07, Stockholm.

668   Johannesson, L-E., Börgesson, L., Goudarzi, R., Sandèn, T., Gunnarsson, D., and Svemar, C.,

669   (2007) "Prototype repository: A full scale experiment at Äspö HRL". *Physics and Chemistry*

670   *of the Earth*, 32, 58-76.

671   Johannesson, L-E., Börgesson, L., and Sandén, T., (1999) *Äspö HRL - Backfill materials*

672   *based on crushed rock (part 2). Geotechnical properties determined in laboratory*, SKB,

673   IPR-99-23, Stockholm.

674   Johannesson, L-E., Gunnarsson, D., Sandén, T., Börgesson, L., and Karlzén, R., (2004) *Äspö*

675   *Hard Rock Laboratory, Prototype Repository, Installation of buffer, canisters, backfill and*

676   *instruments in section II*, SKB, IPR-04-13, Stockholm.

677   Lloret, A., Villar, M.V., Sánchez, M., Gens, A., Pintado, X., and Alonso, E.E., (2003)

678   "Mechanical behaviour of heavily compacted bentonite under high suction changes",

679   *Géotechnique*, 53(1), 27-40.

680   Masum, S.A., Vardon, P.J., Thomas, H.R., Chen, Q., and Nicholson, D., (2012)

681   "Multicomponent gas flow through compacted clay buffer in a higher activity radioactive

682   waste geological disposal facility", *Mineralogical Magazine*, 76 (8), 3337-3344.

683   Mata, C., (2003) *Hydraulic behaviour of bentonite based mixtures in engineered barriers:*

684   *The Backfill and Plug Test at the Äspö HRL (Sweden)*, PhD Thesis, Technical University of

685   Catalonia, Barcelona.

686 Mishra, S.B., Nagaraj, C., Venkateswarlu, V., and Adhikari, G.R., (2008) "Measurement and

687 analysis of pore water pressure in large caverns and shafts in a hydro-electric project",

688 *Geotechnical and Geological Engineering*, 26, 367-374.

689 Patel, S., Dahlström, L-O., and Stenberg, L., (1997) *Äspö Hard Rock Laboratory,*

690 *Characterisation of the rock mass in the prototype repository at Äspö HRL stage 1*. SKB,

691 HRL-97-24, Stockholm.

692 Pusch, R., (2001) *The buffer and backfill handbook, Part 2: Materials and techniques*, SKB,

693 TR-02-12, Stockholm.

694 Rhén, I., and Forsmark, T., 2001. *Äspö Hard Rock Laboratory, Prototype Repository,*

695 *Summary report of investigations before the operation phase*. SKB, IPR-01-65, Stockholm.

696 Rhén, I., Gustafson, G., Stanfors, R., and Wikberg, P., (1997) *Äspö HRL - Geoscientific*

697 *evaluation 1997/5, Models based on site characterization 1986-1995*. SKB, TR-97-06,

698 Stockholm.

699 Stille, H., and Olsson, P., (1996) *Summary of rock mechanical results from the construction*

700 *of Äspö Hard Rock Laboratory*, SKB, HRL-96-07.

701 Svemar, C., and Pusch, R., (2000) *Äspö Hard Rock Laboratory, Prototype Repository,*

702 *Project description*, SKB, IPR-00-30, Stockholm.

703 Thomas, H.R., Cleall, P.J., Chandler, N., Dixon, D., and Mitchell, H.P., (2003) "Water

704 infiltration into a large-scale in-situ experiment in an underground research laboratory",

705 *Géotechnique*, 53(2), 207-224.

706 Thomas, H.R., Cleall, P.J., Dixon, D., and Mitchell, H.P., (2009) "The coupled thermal-

707 hydraulic-mechanical behaviour of a large-scale in situ heating experiment", *Géotechnique*,

708 59(4), 401-413.

709 Thomas, H.R., and He, Y. (1997), "A coupled heat-moisture transfer theory for deformable

710 unsaturated soil and its algorithmic implementation". *International Journal of Numerical*

711 *Methods in Engineering*, 40, 3421-3441.

712 Thomas, H.R., and He, Y., (1998) "Modelling the behaviour of unsaturated soil using an

713 elasto plastic constitutive relationship", *Géotechnique*, 48(5), 589-603.

714 Thomas, H.R., Sedighi, M., and Vardon, P.J., (2012) "Diffusive Reactive Transport of

715 Multicomponent Chemicals under Coupled Thermal, Hydraulic, Chemical and Mechanical

716 (THCM) Conditions", *International Journal of Geomechanics,* 30(4), 841-857.

717 Thorsager, P., Börgesson, L., Johannesson, L., and Sandén, T., (2002) *Canister Retrieval*

718 *Test, Report on installation*, SKB, IPR-02-30, Stockholm.

719 Vardon, P.J., (2009) *A three-dimensional numerical investigation of the thermo-hydro-*

720 *mechanical behaviour of a large-scale prototype repository*, PhD Thesis, Cardiff University,

721 Cardiff.

722 Vardon, P.J., Cleall, P.J., Thomas, H.R., Philp, R.N., and Banicescu, I., (2011) "Three-

723 dimensional field-scale coupled Thermo-Hydro-Mechanical modelling: a parallel computing

724 implementation". *ASCE International Journal of Geomechanics*, 11(2), 90-99.

725 Villar, M.V., Martín, P.L., Barcala, J.M., (2005) *Infiltration tests at isothermal conditions*

726 *and under thermal gradient*, CIEMAT, Technical Report CIEMAT/DMA /M2140/1/05,

727 Madrid.

728

729

755   Figure 9. Contour plots of temperature (K) variation in the simulation.

756   Figure 10. Contour plots of pore-water pressure (Pa) variation in the simulation (DH-1 to

757   DH-4).

758   Figure 11. Contour plots of displacement (m) variation in the simulation (DH-1 to DH-4).

759   Figure 12. Contour plots of pore-water pressure (Pa) variation in the simulation in a

760   horizontal cross section intersecting the tunnel.

761

762

763   Table 1. Preliminary fracture model data, including initial hydraulic conductivity estimates

764   for the fractures, items marked * after Rhén and Forsmark (2001).

Feature	East*	North*	Z*	Strike*	Dip*	Radius*	Tr*	Thickness[b]	Hydraulic Conductivity[c], K_{feat}	Analysis Hydraulic Conductivity, K_{feat}
	(m)	(m)	(mamsl[a])	(°)	(°)	(m)	(m²/s)	(m)	(m/s)	(m/s)
Intact rock										1.0×10^{-11}
Major features										
North Major*	1 892	7 289	-449	118	88	20	$5\text{-}10 \times 10^{-8}$	0.1	$5\text{-}10 \times 10^{-7}$	8×10^{-7}
South Major*	1 887	7266	-449	124	89	20	$7\text{-}9 \times 10^{-8}$	0.1	$7\text{-}9 \times 10^{-7}$	8×10^{-7}
Region 1										8×10^{-7}
Minor features										
3587/1*	1 878.28	7 275.03	-453.53	354	79	2	8.1×10^{-9}	0.05	1.62×10^{-7}	1.6×10^{-7}
3551/1*	1 915.42	7 271.06	-455.24	312	40	2	4.7×10^{-9}	0.05	9.4×10^{-8}	9.4×10^{-8}
3551/2*	1 917.50	7 269.90	-455.56	271	38	2	3.3×10^{-9}	0.05	6.6×10^{-8}	6.6×10^{-8}
3545/1*	1 919.55	7 268.80	-453.54	164	64	2	2.8×10^{-10}	0.05	5.6×10^{-9}	5.6×10^{-9}
3545/2*	1 919.55	7 268.80	-456.66	278	24	2	1.7×10^{-9}	0.05	3.4×10^{-8}	3.4×10^{-8}
3545/3*	1 921.45	7 270.22	-453.14	298	64	2	1.3×10^{-8}	0.05	2.6×10^{-7}	2.6×10^{-7}

[a]*metres above mean sea level*, [b]*assumed*, [c]*derived*
East, North and Z are all coordinates in the Äspö coordinate system and Tr is the transmissivity.

765

766

Table 2. Material parameters

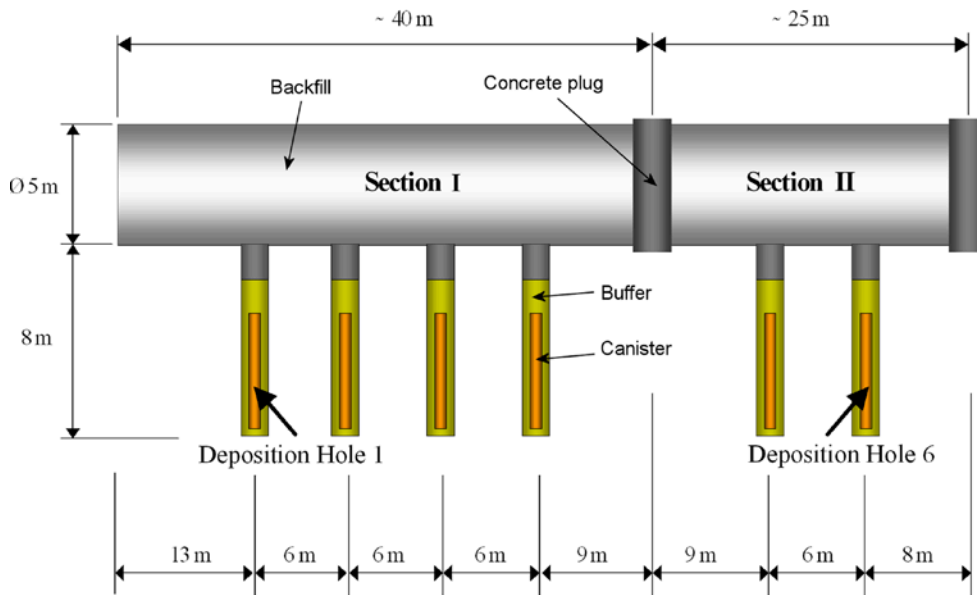| Properties	Rock	Fractures	MX-80 buffer	MX-80 pellets	Backfill	Concrete
Porosity, n	0.005	0.1	0.4 cylinders, 0.36 rings, 0.384 bricks	0.61	0.363	0.005
ρ_s (kg/m^3)	2770	2770	2780	2780	2780	2770
Heat capacity of solid, C_{ps}	750	750	800	800	850	750
λ_T (W/mK)	2.5	2.5	0.3-1.3 as equation 1	0.3-1.3 as equation 1	0.3-1.5 as equation 2	2.5
K_l (m/s)	$K_l = K_{sat}S_l^{0.5}(1-(1-S_l^{1/\beta_l})^{\beta_l})^2$	As rock	$K_{swell} = K_{sat}(S_l)^\delta(1-\omega_{abs}S_l)$ $\frac{\partial \omega_{abs}}{\partial t} = \alpha - \frac{S_{labs}}{S_l^2}\frac{\partial S_l}{\partial t}$ where $\omega_{abs} < \omega_{abs}^{max}$ and $S_l < 1$	$K_{pel} = (1-\omega_{pel})k_{init} + k_{inf}\omega_{pel}$ $\frac{\partial \omega_{pel}}{\partial t} = \beta_p$	$K_l = K_{sat}S_l^\delta$	As rock
Constants	$K_{sat} = 5.0 \times 10^{-12}$	K_{sat} = various	$K_{sat} = 1.9 \times 10^{-14}$ $\alpha_l = 1.0 \times 10^{-7}$ $\delta = 3$	$k_{init} = 1.0 \times 10^{-10}$ $k_{inf} = 1.0 \times 10^{-16}$ $\beta_p = 1.0 \times 10^{-7}$	$K_{sat} = 1.5 \times 10^{-10}$ $\delta = 10$	$K_{sat} = 1.0 \times 10^{-14}$
S_l	$S_l = \left(1+\left[\frac{s}{P_0}\right]^{1/1-\beta_l}\right)^{-\beta_l}$	As rock	$nS_l = \theta_{res} + \frac{\theta_{sat}-\theta_{res}}{\left(1+\left[\frac{1000\alpha s}{\rho_l g}\right]^b\right)^{(1-1/b)}}$	As MX-80 buffer	As MX-80 buffer	As rock
Constants	$\beta = 0.33$ $P_0 = 0.33$ (Pa^{-1})	$\beta = 0.33$ $P_0 = 0.33$	$\alpha = 1.25 \times 10^{-7}$ (m^{-1}) $b = 1.75$ $\theta_{res} = 0.0001$ $\theta_{sat} = n$	$\alpha = 7.00 \times 10^{-6}$ $b = 1.30$ $\theta_{res} = 0.0001$ $\theta_{sat} = n$	$\alpha = 1.00 \times 10^{-4}$ $b = 1.23$ $\theta_{res} = 0.0001$ $\theta_{sat} = n$	$\beta = 0.33$ $P_0 = 0.33$
	Initial condition, $S_l=1$		Initial conditions (cylinders, rings, bricks), $S_l=0.79, 0.86, 0.64$	Initial condition, $S_l=0.25$	Initial condition, $S_l=0.524$	Initial condition, $S_l=1$
G (MPa)	27600	27600	10	1	10	27600
υ	0.25	0.25	-	-	-	0.25
κ	-	-	0.0245	0.25	0.016	-
$\lambda(0)$	-	-	0.238	0.6	0.102	-
p_c (MPa)	-	-	1.0×10^5	1.0×10^5	1.0×10^5	-
p_0^* (MPa)	-	-	45	45	45	-
β	-	-	1.0	1.0	1.0	-
r	-	-	0.9	0.9	0.9	-
M	-	-	0.358	0.358	0.358	-
k	-	-	5.6×10^{-3}	5.6×10^{-3}	1.7×10^{-3}	-
κ_s	-	-	0.075	0.075	0.025	-
α_T (K^{-1})	8.0×10^{-6}	8.0×10^{-6}	1.0×10^{-4}	1.0×10^{-4}	3.56×10^{-5}	8.0×10^{-6}

768

769

770

771

Figure 1. Schematic of the PRP project (after Svemar and Pusch, 2000).

772

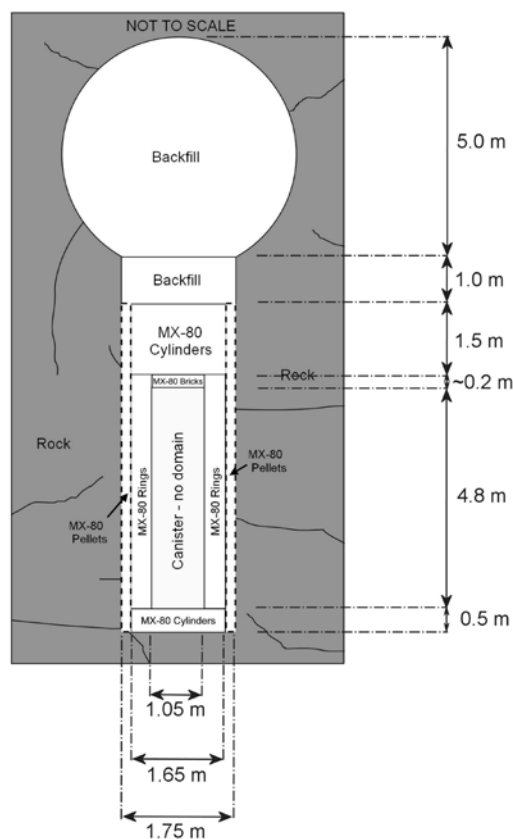773   Figure 1. Schematic of the PRP project (after Svemar and Pusch, 2000).

Figure 2. Materials contained within the repository.

774

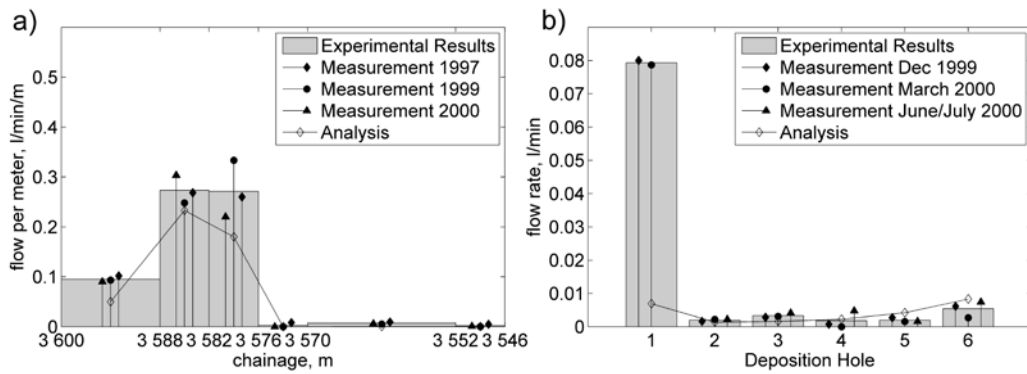775   Figure 2. Materials contained within the repository.

Figure 3. Tunnel and deposition-hole inflow measurements. a) Experimental data for the tunnel inflow (after Rhén and Forsmark, 2001) and the numerical results; b) Experimental data for the inflow into the deposition-holes (after Rhén and Forsmark, 2001) and the numerical results.

776

777   Figure 3. Tunnel and deposition-hole inflow measurements. a) Experimental data for

778   the tunnel inflow (after Rhén and Forsmark, 2001) and the numerical results;   b)

779   Experimental data for the inflow into the deposition-holes (after Rhén and Forsmark,

780   2001) and the numerical results.

781
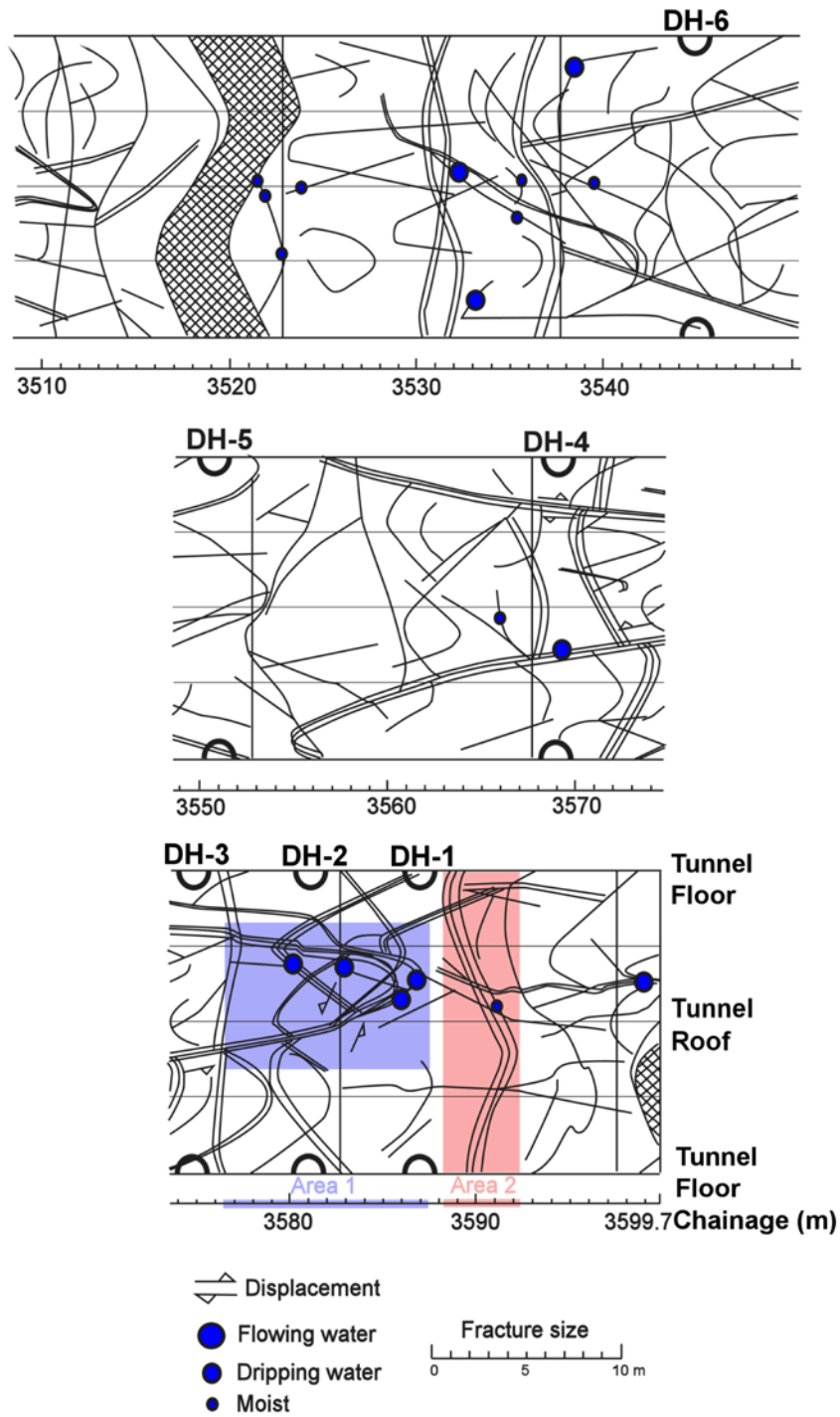
Figure 4. Fracture map of along the tunnel, where the centreline is the roof (after Rhén and Forsmark, 2001). Water bearing structures are identified throughout as circles and two areas of large inflows are highlighted as 'Area 1' and 'Area 2'.

782

783   Figure 4. Fracture map of along the tunnel, where the centreline is the roof (after

784   Rhén and Forsmark, 2001).   Water bearing structures are identified throughout as

785   circles and two areas of large inflows are highlighted as '*Area 1*' and '*Area 2*'.

786
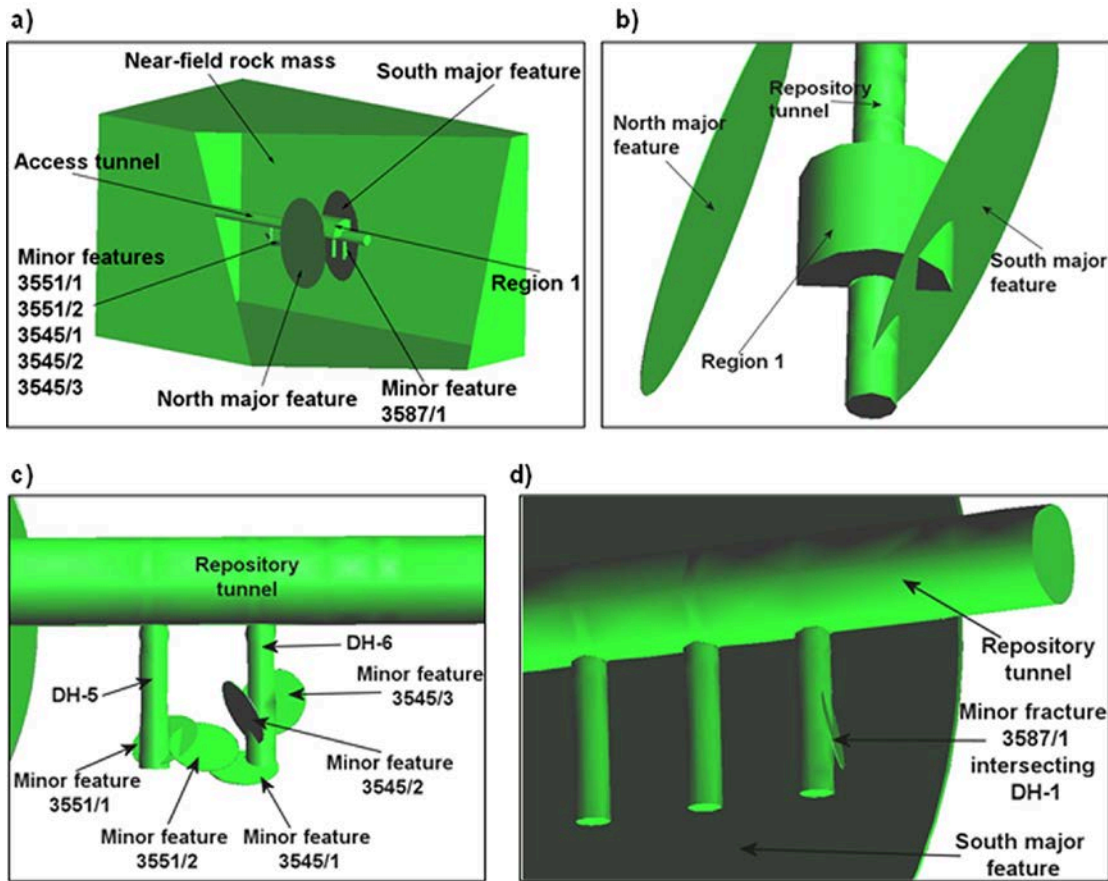
Figure 5. Visualisations of the model domain. a) complete domain; b) view from above the repository tunnel c) detailed view of DH-5 and 6 d) DH-1 to 3.

787

788   Figure 5. Visualisations of the model domain. a) complete domain; b) view from

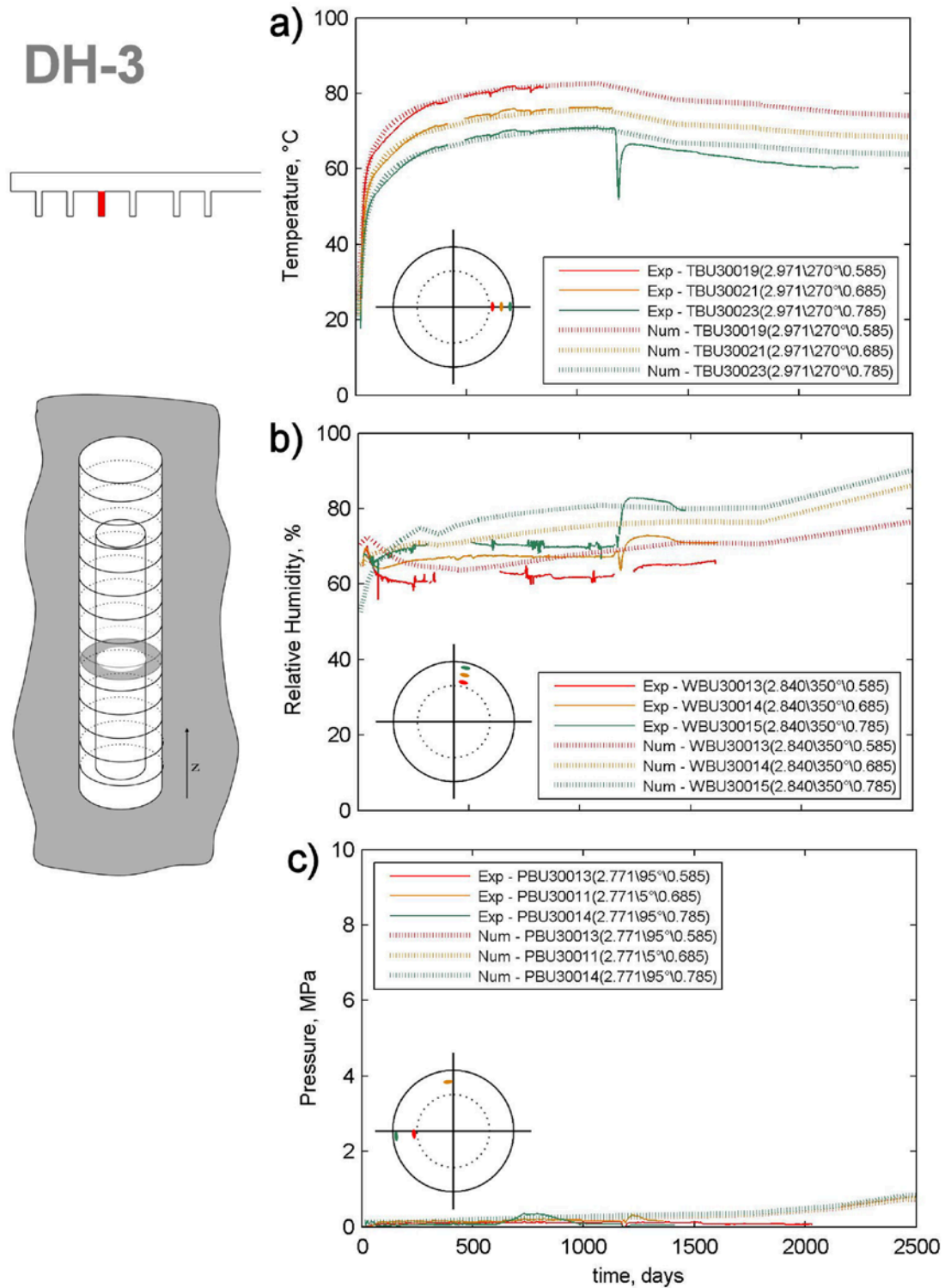789   above the repository tunnel c) detailed view of DH-5 and 6 d) DH-1 to 3.

790
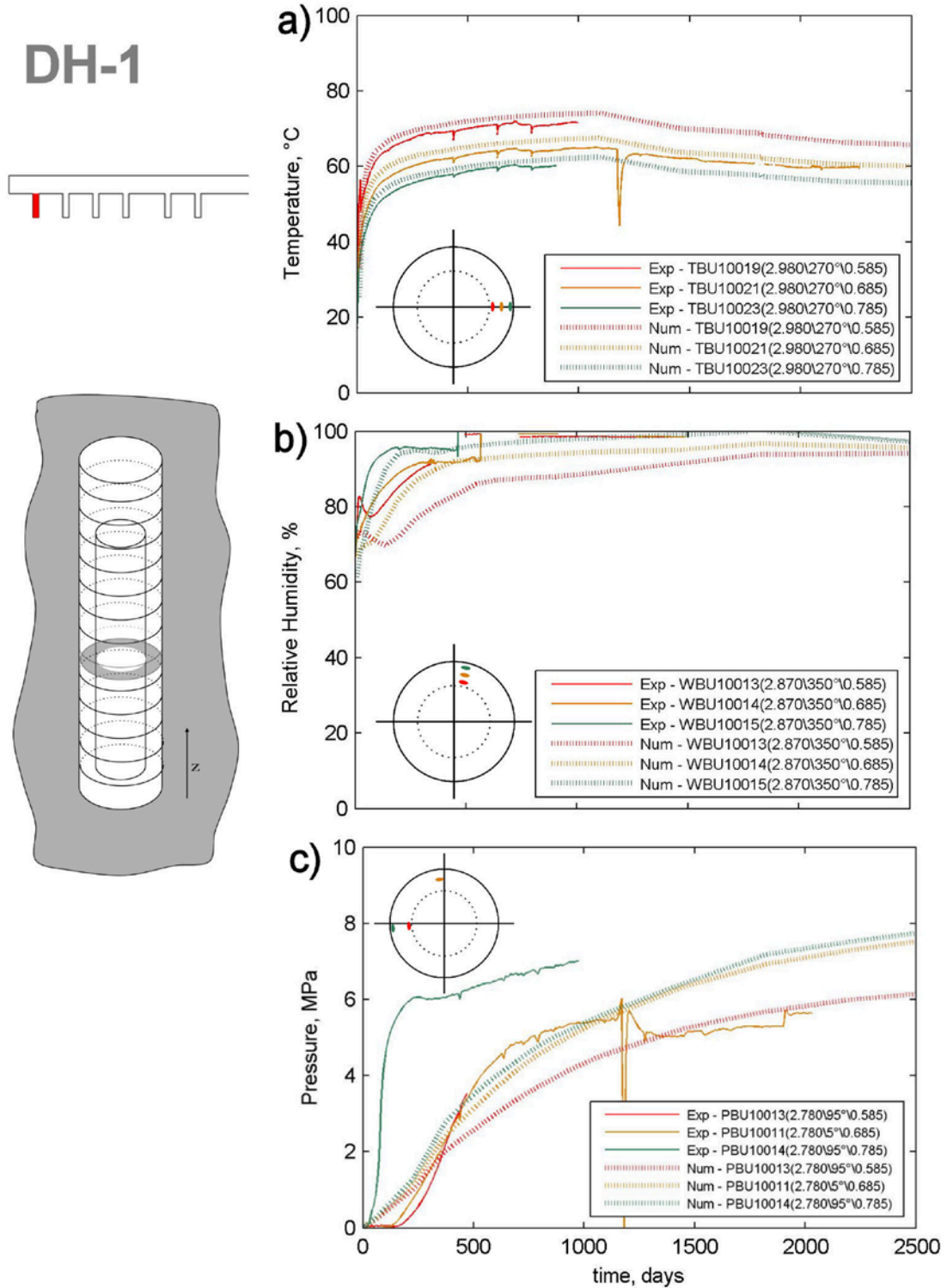
Figure 6. Numerical and experimental results for temperature, relative humidity and net mean stress measurements at mid-height in DH-1. Experimental results after Goudarzi and Johannesson (2007).

Figure 6. Numerical and experimental results for temperature, relative humidity and net mean stress measurements at mid-height in DH-1. Experimental results after Goudarzi and Johannesson (2007).

Figure 7. Numerical and experimental results for temperature, relative humidity and net mean stress measurements at mid-height in DH-3. Experimental results after Goudarzi and Johannesson (2007).

795

796   Figure 7. Numerical and experimental results for temperature, relative humidity and

797   net mean stress measurements at mid-height in DH-3. Experimental results after

798   Goudarzi and Johannesson (2007).
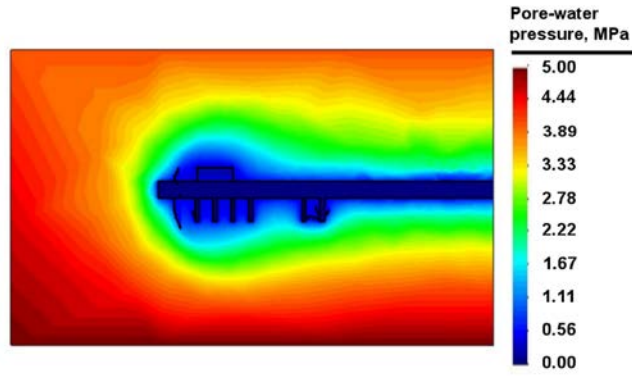
Figure 8. Contour plot of results from pre-placement analysis complete with discrete fractures in the model domain.

799

800 Figure 8. Contour plot of results from pre-placement analysis complete with discrete

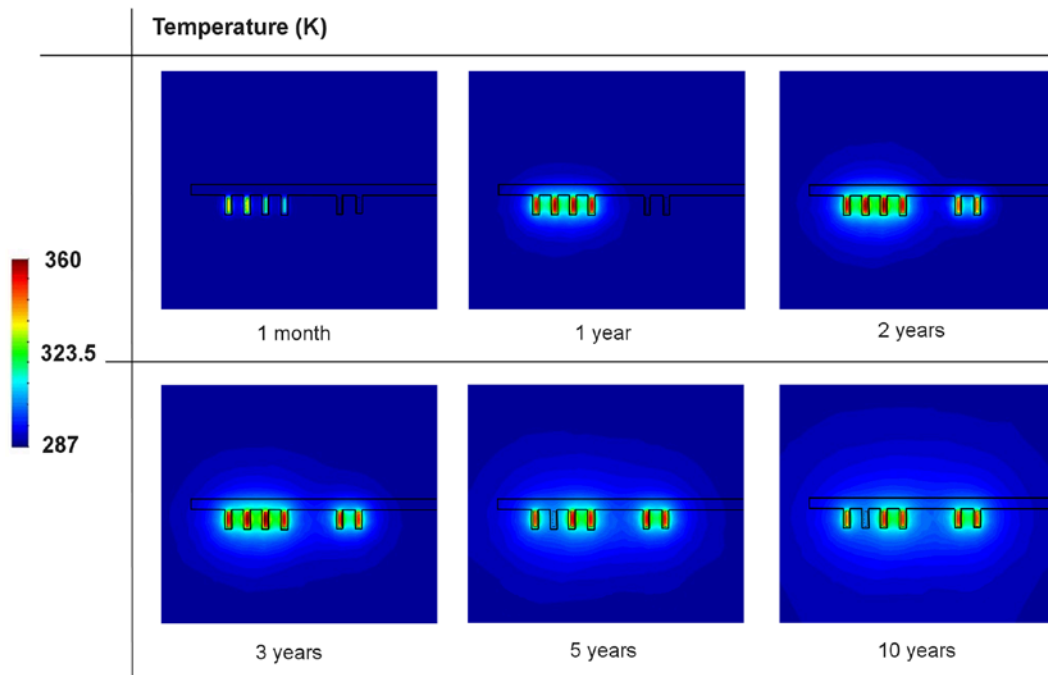801 fractures in the model domain.

802

Figure 9. Contour plots of temperature (*K*) variation in the simulation.

803

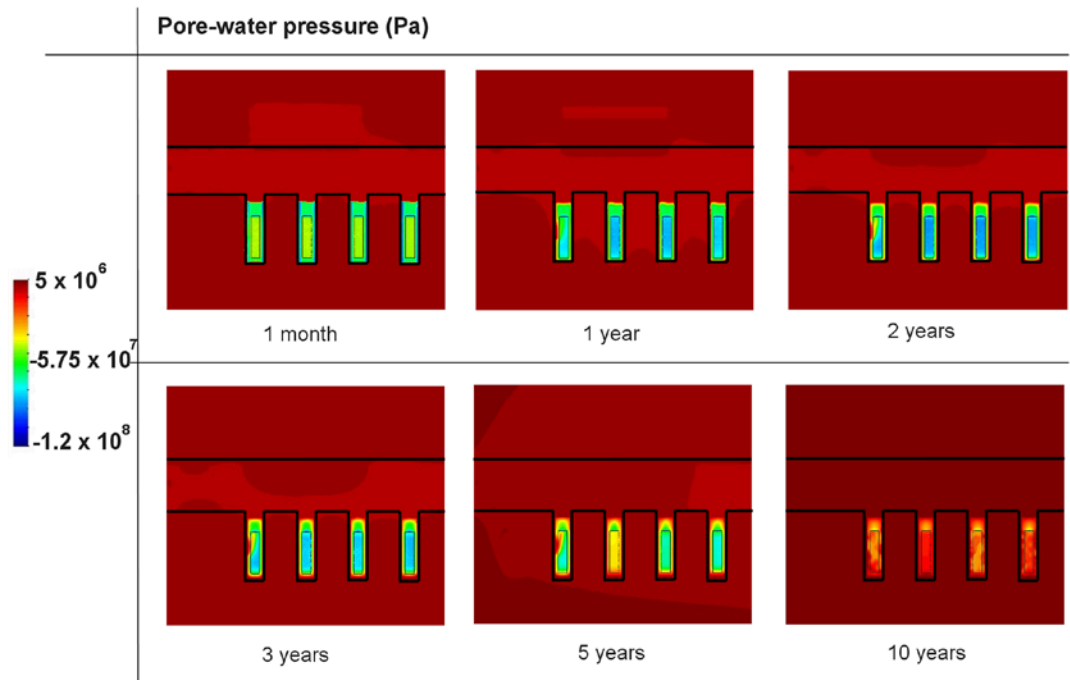804 Figure 9. Contour plots of temperature (*K*) variation in the simulation.

805

Figure 10. Contour plots of pore-water pressure (*Pa*) variation in the simulation (DH-1 to DH-4).

806

807   Figure 10. Contour plots of pore-water pressure (*Pa*) variation in the simulation (DH-
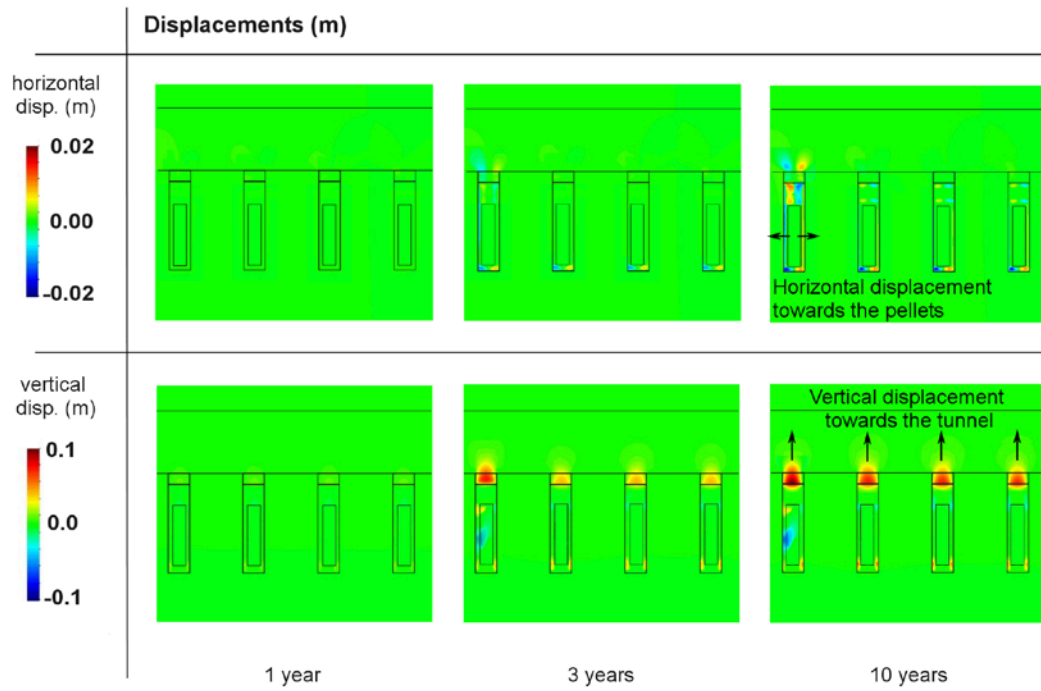
808   1 to DH-4).

809

Figure 11. Contour plots of displacement (*m*) variation in the simulation (DH-1 to DH-4).

810

811   Figure 11. Contour plots of displacement (*m*) variation in the simulation (DH-1 to
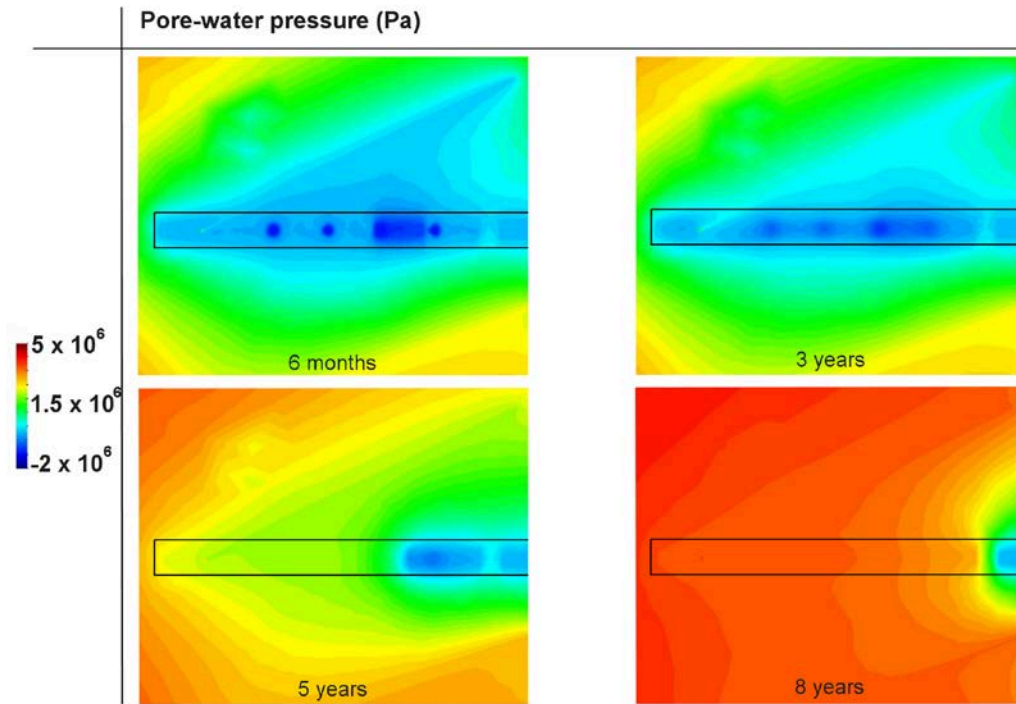
812   DH-4).

813

Figure 12. Contour plots of pore-water pressure (*Pa*) variation in the simulation in a horizontal cross section intersecting the tunnel.

814

815 Figure 12. Contour plots of pore-water pressure (*Pa*) variation in the simulation in a

816 horizontal cross section intersecting the tunnel.

817